

Magnetic and Lattice Ordered Fractional Quantum Hall Phases in Graphene

Jincheng An,^{1,*} Ajit C. Balram^{2,3,†} and Ganpathy Murthy^{1,‡}

¹*Department of Physics and Astronomy, University of Kentucky, Lexington, KY 40506, USA*

²*Institute of Mathematical Sciences, CIT Campus, Chennai, 600113, India*

³*Homi Bhabha National Institute, Training School Complex, Anushaktinagar, Mumbai 400094, India*

At and near charge neutrality, monolayer graphene in a perpendicular magnetic field is a quantum Hall ferromagnet. In addition to the highly symmetric Coulomb interaction, residual lattice-scale interactions, Zeeman, and sublattice couplings determine the fate of the ground state. Going beyond the simplest model with ultra-short-range residual couplings to more generic couplings, one finds integer phases that show the coexistence of magnetic and lattice order parameters. Here we show that fractional quantum Hall states in the vicinity of charge neutrality have even richer phase diagrams, with a plethora of phases with simultaneous magnetic and lattice symmetry breaking.

Introduction.—The integer [1, 2] and fractional [3–6] quantum Hall effects are the earliest known topological insulators [7, 8]. The bulk has a charge gap, with the protected chiral edge modes [9] being responsible for electrical transport. When internal degeneracies such as spin or valley are present, interactions lead to quantum Hall ferromagnetism [10–13]. While the discovery of the integer/fractional quantum Hall effects (IQHEs/FQHEs) took place in semiconductor heterostructures, graphene [14–18] emerged in the early 2000’s as an alternate platform. In the absence of a perpendicular magnetic field B_{\perp} , monolayer graphene, with its honeycomb structure, has two Dirac band crossings at the corners of the Brillouin Zone, the K and K' points. For realistic B_{\perp} fields, each Dirac point manifests a set of particle-hole symmetric Landau levels (LLs) with energies $E_n \propto \text{sgn}(n) \sqrt{|n|B_{\perp}}$. The $n=0$ LL is special, with the wave function in each valley being restricted to one sublattice, a phenomenon known as valley-sublattice locking. The $n=0$ manifold of four (two for spin and two for valley) nearly degenerate LLs [called the zero-LLs (ZLLs)] has proven to be a fascinating example of quantum Hall ferromagnetism, one that is not yet fully understood. The charge neutral state, with two linear combinations of the four ZLLs filled, is labeled $\nu=0$. This state [17, 19–28], and nearby fractional fillings have attracted a lot of attention experimentally [25, 29–36].

Based on a large body of work [37–42], a simple model Hamiltonian in the ZLLs was proposed by Kharitonov [43]. The long-range Coulomb interaction is $SU(4)$ symmetric in the spin-valley space, and ultra-short-range (USR) residual interactions encode all the anisotropies. In the Hartree-Fock (HF) approximation, the ground state at $\nu=0$ breaks either the lattice symmetries or the $U(1)$ spin-rotation symmetry around the total field, but not both [43]. Experimentally, there is strong evidence from scanning tunneling microscopy (STM) experiments [26–28, 44, 45] and magnon transmissions studies [22–25] that the ground states at $\nu=0$ and fractions around it spontaneously break both magnetic and lattice symme-

tries simultaneously. Relaxing the USR condition leads to ground states that do show the coexistence of spontaneous lattice and magnetic symmetry breaking [46–48].

A variational approach based on USR anisotropic interactions was proposed by Sodemann and MacDonald for FQH states in the ZLLs [49]. For USR interactions, only the relative angular momentum $m=0$ Haldane pseudopotential V_0 [50] is nonzero, which leads to a HF-like variational energy for the FQH state in the ZLLs [49]. Spontaneous breaking of lattice *and* magnetic order seems to be extremely rare in this analysis or extensions thereof [51]. In this Letter, we will explain the coexistence of lattice and magnetic orders in the most robust fractions in the vicinity of charge neutrality [22–28, 44, 45] by analyzing a more generic set of residual interactions that have a nonzero range. Specifically, we will show that when the residual anisotropic interactions have nonzero V_0 and V_1 , a rich phase diagram with multiple regions of coexistence between spontaneously broken lattice and magnetic orders is obtained, especially in what is believed to be the physical regime of parameters. The introduction of nonzero-range interactions is motivated by physics. (i) From the renormalization group point of view, given the sizeable LL mixing, integrating out the other $|n|>0$ manifolds will inevitably generate nonzero range interactions [46, 47]. (ii) In Bernal-stacked bilayer graphene, which has many of the same phases as monolayer graphene [36, 52], trigonal warping can induce nonzero range effective interactions [53, 54]. (iii) Projecting a USR interaction to a higher $|n|\neq 0$ Landau level manifold will also result in such interactions [55]. (iv) In the IQHE for $\nu=\pm 1$, nonzero-range interactions are crucial in breaking unphysical degeneracies [56–58] and providing a spin-valley stiffness.

Hamiltonian and variational states.—We include the Zeeman coupling E_z and a sublattice symmetry breaking/valley Zeeman coupling E_v induced by the moiré potential of the encapsulating hexagonal Boron Nitride (hBN) [59–62]. In addition to the $SU(4)$ symmetric Coulomb interaction, a generic interacting Hamiltonian

in the ZLLs has the following residual anisotropic inter-

$$H^{\text{an}} = \frac{1}{2} \int d^2\mathbf{r}_1 d^2\mathbf{r}_2 \sum_{i,\alpha,\beta,\gamma,\delta} : \hat{\psi}_\alpha^\dagger(r_1) \tau_i^{\alpha\beta} \hat{\psi}_\beta(r_1) V_i(r_1 - r_2) \hat{\psi}_\gamma^\dagger(r_2) \tau_i^{\gamma\delta} \hat{\psi}_\delta(r_2) : , \quad (1)$$

where $i=x, y, z$, $V_x=V_y=V_\perp(r_1-r_2)$, $\alpha, \beta, \gamma, \delta$ run over all the spin and valley indices, and the electron operators have been projected to the $n=0$ LL. We abstractly define

$$\mathcal{V}_i = (g_{0i}\mathcal{P}_0 + g_{1i}\mathcal{P}_1) : \hat{\tau}_i \hat{\tau}_i : , \quad (2)$$

where \mathcal{P}_m represents a two-body interaction projected to the relative angular momentum m state, and g_{0i}, g_{1i} are numbers with energy units. The Hartree and Fock couplings associated to these are $g_{i,H}=g_{0i}+g_{1i}$, $g_{i,F}=g_{0i}-g_{1i}$ [63]. It is widely believed [27, 43] that for real samples, $g_z > 0$, $g_\perp < 0$, with their magnitudes not too different from each other.

The interaction terms have the symmetry $SU(2)_s \otimes U(1)_v \otimes Z_{2v}$ [37], where the subscripts s, v stand for spin and valley respectively. Upon adding E_z , E_v , the Hamiltonian has the symmetry $U(1)_s \otimes U(1)_v$. Upon the inclusion of 6-fermion terms, the $U(1)_v$ breaks down to a Z_{3v} . Thus, the spontaneous symmetry breaking of $U(1)_v$ (at the 4-fermion level) does not lead to Goldstone modes. We examine nonzero averages of the following one-body operators, written schematically as σ_z [ferromagnet (FM)], $\tau_z \sigma_x$ [canted antiferromagnet (CAF)], τ_z [charge-density-wave (CDW)], τ_x [often termed Kekulé distorted (KD)], but we use the more general term bond-ordered (BO)], $\tau_x \sigma_x$ [spin-valley entangled-X (SVEEX)], $\tau_y \sigma_y$ (SVEY), and $\tau_z \sigma_z$ [antiferromagnet (AF)].

We focus upon the filling $\nu = -2 + 5/3$, which has been studied by variational [49] and exact diagonalization methods [64–67], albeit only for USR interactions. We will see how the introduction of V_1 immediately leads to states manifesting the simultaneous spontaneous breaking of magnetic and lattice symmetries. We use a generalization of a previously used ansatz [49, 57, 68, 69]. Any 4-component spinor can be written in a basis of direct products of 2-component spinors in the valley and spin spaces, denoted by $|\mathbf{n}\rangle \otimes |\mathbf{s}\rangle \equiv |\mathbf{n}, \mathbf{s}\rangle$. For example, for $\mathbf{s} = \sin(\theta_s) [\cos(\phi_s) \hat{e}_x + \sin(\phi_s) \hat{e}_y] + \cos(\theta_s) \hat{e}_z$, $|\mathbf{s}\rangle = [\cos(\theta_s/2), e^{i\phi_s} \sin(\theta_s/2)]^T$, and $|\mathbf{-s}\rangle$ is obtained by $\theta \rightarrow \pi - \theta$, $\phi \rightarrow \phi + \pi$ [details in the Supplemental Material (SM) [63]]. We can use the $U(1)$ symmetries to rotate \mathbf{n}, \mathbf{s} so that they lie in the xz -plane, reducing the freedom to two angles $\theta_n, \theta_s \in [0, \pi]$, while ϕ_n and ϕ_s is either 0 or π . We will need up to four spinors, either fully or

actions:

partially occupied. We define

$$\begin{aligned} |f_1\rangle &= \cos(\alpha_1/2) |\mathbf{n}, \mathbf{s}_a\rangle + \sin(\alpha_1/2) |-\mathbf{n}, -\mathbf{s}_b\rangle \\ |f_2\rangle &= \cos(\alpha_2/2) |\mathbf{n}, -\mathbf{s}_a\rangle + \sin(\alpha_2/2) |-\mathbf{n}, \mathbf{s}_b\rangle \\ |f_3\rangle &= \sin(\alpha_1/2) |\mathbf{n}, \mathbf{s}_a\rangle - \cos(\alpha_1/2) |-\mathbf{n}, -\mathbf{s}_b\rangle \\ |f_4\rangle &= \sin(\alpha_2/2) |\mathbf{n}, -\mathbf{s}_a\rangle - \cos(\alpha_2/2) |-\mathbf{n}, \mathbf{s}_b\rangle, \end{aligned} \quad (3)$$

where $\mathbf{s}_a, \mathbf{s}_b$ are, in general, different, and α_1, α_2 are introduced to cover a bigger range of variational states. We now have five continuously varying angles, $\theta_n, \theta_a, \theta_b, \alpha_1, \alpha_2$, and additionally the discrete possibilities $0, \pi$ for ϕ_n and ϕ_s . This turns out to be sufficient to describe the most general two-component states (2CSs). For three-component states (3CSs), we need to take further linear combinations of the $|f_i\rangle$ to capture the full range of possibilities, as is detailed in the SM [63].

Variational states: We use the composite fermion (CF) theory to construct variational FQHE states. According to the CF theory, the FQHE state at $\nu = n/(2n \pm 1)$ maps into the $\nu^* = n$ IQHE state of CFs, which are electrons bound to two vortices [70]. In the presence of (pseudo)spin, $n = n_\uparrow + n_\downarrow$, where n_\uparrow (n_\downarrow) is the number of filled spin-up (spin-down) CF-LLs. This state, denoted by $[n_\uparrow, n_\downarrow]_{\pm 2}$ [71], is an eigenstate of the total spin and is described by the Jain wave function $\Psi_{n/(2n \pm 1)}^{[n_\uparrow, n_\downarrow]_{\pm 2}} = \mathcal{P}_{\text{LLL}} \Phi_{\pm n_\uparrow} \Phi_{\pm n_\downarrow} \prod_{j < k} (z_j - z_k)^2$, where the complex coordinate z_j parametrizes the position of the j th electron, Φ_n is the Slater determinant wave function of n filled LLs ($\Phi_{-|n|} = [\Phi_{|n|}]^*$), and \mathcal{P}_{LLL} denotes projection into the LLL. Unless otherwise stated, we shall use the ground states obtained from the exact diagonalization of the bare Coulomb interaction in the LLL to represent the CF states since for all accessible systems the two have a near unit overlap with each other [72–78].

For $\nu = 2/3$, we shall consider the fully polarized $[2, 0]_{-2}$ and the singlet $[1, 1]_{-2}$ states. The $[2, 0]_{-2}$ state is nearly identical to the state obtained by hole conjugating the $1/3$ Laughlin state [78, 79] and since the latter can be treated semi-analytically, we shall use this representation for it. Using the fact that the $1/3$ Laughlin state has $\langle V_1 \rangle = 0$ and the $\nu = 1$ state has $\langle V_1/N_\phi \rangle = 2$ in the thermodynamic limit, where N_ϕ is the number of flux quanta, one can show that the fully polarized $2/3$ state has $\langle V_1/N_\phi \rangle = 2/3$ in the thermodynamic limit [63]. For the singlet state, by extrapolating finite system results in the spherical geometry [50] we numerically obtained $\langle V_0/N_\phi \rangle = 0.001$ and $\langle V_1/N_\phi \rangle = 0.49153$ in the thermody-

dynamic limit [63]. Furthermore, the singlet state has $\langle V_1^{\uparrow,\uparrow} \rangle = \langle V_1^{\uparrow,\downarrow} \rangle = \langle V_1^{\downarrow,\downarrow} \rangle$ [63], where $V_m^{\sigma,\sigma'}$ is the V_m pseudopotential energy for two electrons, one with spin σ and the other with spin σ' . Since the singlet state has a very small $\langle V_0/N_\phi \rangle$ we can safely assume it to be hard-core (keeping a factor of $\prod_{j<k} (z_j - z_k)$ outside \mathcal{P}_{LLL} in $\Psi_{2/3}^{[1,1]-2}$ explicitly makes the state hard-core [74]) since its small V_0 component will modify the phase boundaries only slightly. In the LLL, the singlet state has a lower bare Coulomb energy than the fully polarized state [80]. We do not consider the direct product of two $1/3$ Laughlin states since that has a much higher Coulomb energy than the fully polarized and singlet $2/3$ states [81].

Results.—We will consider two candidate states for $-2+5/3$: $(1, [2, 0]_{-2}, 0)$ and $(1, [1, 1]_{-2}, 0)$ (identical to $(1, 2/3, 0, 0)$ and $(1, 1/3, 1/3, 0)$ of Ref. [49] respectively). The first is a 2CS, while the second is a 3CS. The non-USR nature of the interactions will be quantified by the parameters $\Delta_i = 2g_{1i}$, where $i=z, \perp$ and g_{1i} is the strength of the $m=1$ pseudopotential appearing in Eq. (2).

Fig. 1(a) shows the phase diagram for the 2CS at $E_z=1$, $E_v=0$, with $\Delta_z=0.5$, $\Delta_\perp=0.7$, corresponding to a sample highly misaligned with the encapsulating hBN to suppress E_v (or even a suspended sample) in a large tilted magnetic field B . In addition to the FM, BO, CDW, CAF, and AF phases known from the variational work with USR interactions [49, 51], we have four additional phases with SVE order, and a tiny sliver of a canted BO (CBO) phase near the boundary between the CDW, CAF, and BO phases. As we show in the SM [63], the SVE phase appears even in the USR limit at $E_v=0$. This result differs from that of Ref. [49], because our variational ansatz [Eq. (3)] is more general. The four SVE phases differ in detail in the type of SVE order they display, and also in which other order parameters are nonvanishing. In phase SVE1, SVEX=SVEY and all other order parameters are nonzero. In phase SVE2, all order parameters are nonvanishing, and SVEX \neq SVEY. In phase SVE3, SVEX and BO orders vanish, but all other order parameters remain nonzero. Finally, in phase SVE4, CDW and SVEX order parameters vanish, but all others remain nonzero. Note that the spinors of both SVE1 and SVE3 are certain limits of the spinors of the KD-AF phase of Ref. [48]. Fig. 1(b) shows a cut through the phase diagram at $g_{z,H}=0.25$. The system is in the BO phase for $g_{\perp,H} < -1$. It crosses an extremely narrow region of the CBO phase near $g_{\perp,H} = -0.45$, one that is better resolved in Fig. 1(c). We emphasize that this is a second-order transition. The system then makes a first-order transition to the CAF phase, which also has nonzero CDW order because of the unequal occupations of the spinors. Around $g_{\perp,H}=0.25$, the system makes a first-order transition into SVE4, which has CAF and BO order as well, but no CDW order. Near $g_{\perp,H}=0.5$ the system finally enters the FM phase via a first-order tran-

sition. Fig. 1(c) shows a section at $g_{z,H} = -0.2$. All order parameters are continuous, implying that all the transitions are second-order. For $g_{\perp,H} < -1$ the system is in the BO phase. As $g_{\perp,H}$ increases it crosses the narrow sliver of the CBO phase and enters the CDW phase, from which it then undergoes a transition to SVE1. After crossing SVE1, it enters SVE2, returns to SVE1, and then enters SVE3. Finally, it exits SVE3 and goes into the FM phase, which also has a nonzero CDW order parameter due to the unequal occupations of the two spinors. The spinors characterizing these phases are explored in the SM [63].

Fig. 2(a) shows the phase diagram of the 3CS for $E_z=1$, $E_v=0$, $\Delta_\perp=0.7$, $\Delta_z=0.5$. We see eight phases in all, as compared to the seven phases seen for USR interactions [49]. These phases are best described in terms of the spinors: $|f_1\rangle$ being fully filled, and $|f_2\rangle$, $|f_3\rangle$ spanning the space forming the singlet. One sees phases such as FM: $|K, \uparrow\rangle$, $|K', \uparrow\rangle$, $|K', \downarrow\rangle$, BO1: $|-\hat{e}_x, \uparrow\rangle$, $|\hat{e}_x, \uparrow\rangle$, $|\hat{e}_x, \downarrow\rangle$, AFCDW1: $|K, \uparrow\rangle$, $|K, \downarrow\rangle$, $|K', \uparrow\rangle$. AFCDW2: $|K, \uparrow\rangle$, $|K, \downarrow\rangle$, $|K', \downarrow\rangle$, CAF: $|K, -\mathbf{s}_a\rangle$, $|K, \mathbf{s}_a\rangle$, $|K', \mathbf{s}_b\rangle$, CBO: $|-\mathbf{n}_a, \uparrow\rangle$, $|\mathbf{n}_a, \uparrow\rangle$, $|\mathbf{n}_b, \downarrow\rangle$. SVE1 with $|K, \uparrow\rangle$, $|K', \downarrow\rangle$, $\cos \frac{\alpha}{2} |K, \downarrow\rangle + \sin \frac{\alpha}{2} |K', \uparrow\rangle$ will have SVEX=SVEY order parameters. SVE2 with all nonzero order parameters has no simple description and has to be found numerically [63].

Fig. 2(b) shows a horizontal cut through the phase diagram at $g_{z,H}=0.25$. The system starts in AFCDW2, makes a second-order transition into CAF, a first-order transition into SVE1, and then transits the FM and CBO phases via second-order transitions to finally end in BO1. Fig. 2(c) shows a vertical cut at $g_{\perp,H}=0.24$. The system starts in the CAF phase and enters SVE2 via a first-order transition, makes a second-order transition into the CBO phase, and finally goes into the FM phase. More details and other parameter choices, including $E_v \neq 0$ for both types of states, are explored in the SM [63].

Conclusions and open questions.—In this Letter, we have shown that given anisotropic interactions beyond USR, the filling $\nu = -2+5/3$ manifests phases that spontaneously break lattice and magnetic symmetries simultaneously. We examined a 2CS [conventionally denoted as $(1, 2/3, 0, 0)$] and a 3CS [denoted $(1, 1/3, 1/3, 0)$]. When sublattice symmetry is present ($E_v=0$), both types of states display rich phase diagrams with several coexistence phases that evolve with E_v [63]. Strong field magnon transport experiments [25] show that fractional states at nonzero E_v develop magnetic order at a critical strength of B_\perp . Very recent STM experiments [44, 45] show lattice symmetry breaking even in FQH states. Though the two types of samples have differences, it seems likely that the spontaneous breaking of lattice and magnetic symmetries occurs simultaneously in all physical samples. Residual anisotropic interactions beyond USR produce such coexistence in large regions of the parameter space and are likely a key ingredient in the

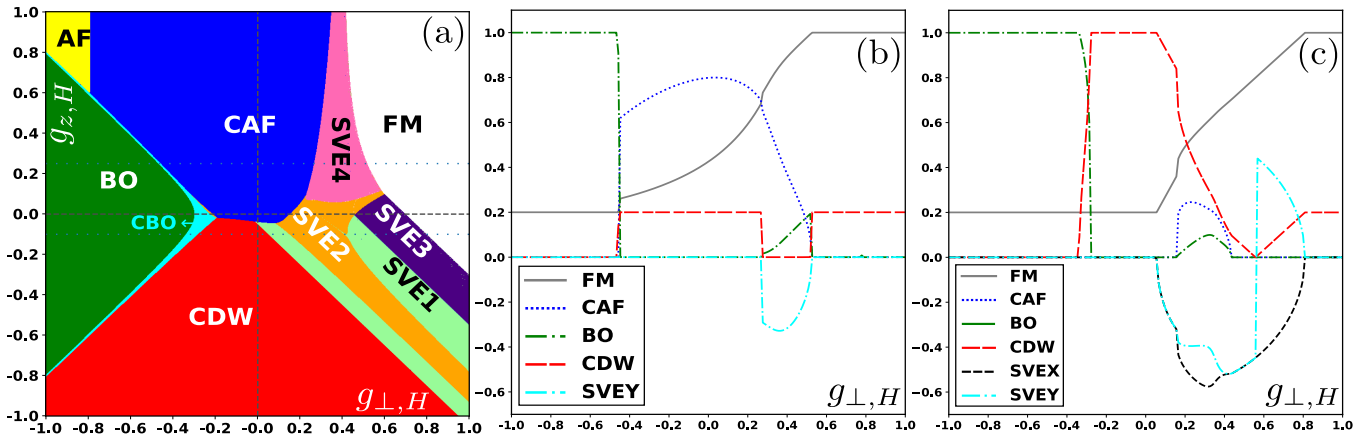


FIG. 1. (a) Phase diagram for the state $(1, [2, 0]_{-2}, 0) \equiv (1, 2/3, 0, 0)$ at $E_z=1$, $E_v=0$, $\Delta_z=0.5$, $\Delta_\perp=0.7$. The SVE phases display a coexistence of magnetic and lattice symmetry breaking. (b) A section through the phase diagram for $g_{z,H}=0.25$ shows how the order parameters behave at the phase boundaries. Both first- and second-order transitions are seen. (c) A section at $g_{z,H}=-0.1$. All the transitions are second-order.

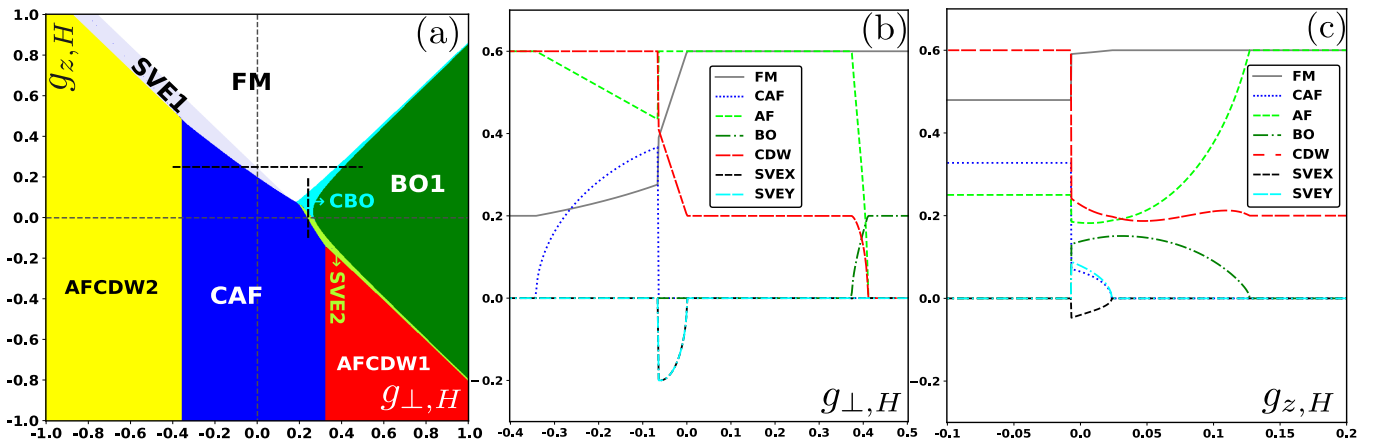


FIG. 2. a) Phase diagram for the state $(1, [1, 1]_{-2}, 0) \equiv (1, 1/3, 1/3, 0)$ at $E_z=1$, $E_v=0$, $\Delta_z=0.5$, $\Delta_\perp=0.7$. Eight different phases are seen, including two SVE phases manifesting a coexistence of lattice and magnetic order. (b) A horizontal section through the phase diagram at $g_{z,H}=0.25$. The system starts in the AFCDW2 phase, enters the CAF via a first-order transition, and then undergoes a second-order transition into the SVE1 phase. Next, it successively traverses the FM and CBO phases before making its way into the BO1 phase. All transitions except the first are second-order. (c) A vertical section at $g_{z,\perp}=0.24$. The system starts in the CAF phase and enters the SVE2 phase via a first-order transition. It then traverses the CBO phase before finally going into the FM phase. The two later transitions are second-order.

correct description of the physics.

A host of open questions remain, such as, how does one uniquely identify a given state experimentally? Electrical and magnon transport [25, 29–36], STM [26–28, 44, 45, 82] including the imaging of order parameters near charged impurities [27], and the detection of the gapless antiferromagnon [83] that characterizes any phase that spontaneously breaks the $U(1)$ spin-rotation symmetry are all important ingredients. Perhaps future spin-polarized STM experiments will be able to directly probe the spin-valley order. In another direction, as B_\perp varies, all short-range couplings except E_v are expected to scale like B_\perp [43]. The Coulomb interaction scales as $\sqrt{B_\perp}$. Thus, even within a particular type of state

(2CS or 3CS) the system can undergo phase transitions as a function of B_\perp . Such transitions have indeed been seen in experiments [20, 25, 36, 84], and their detailed understanding is an important task. Furthermore, due to the difference in Coulomb energy between the 2CSs and 3CSs, transitions may occur between them as B_\perp varies [63]. Extensions of our work include considering nonzero pseudopotentials for higher relative angular momenta or analyzing the phase diagrams of states such as $-2+7/5$ and even-denominator states (seen in graphene [34, 85]). We are actively pursuing efforts in these directions [86].

An important theoretical problem is to quantitatively understand how the residual anisotropic interactions be-

come longer-ranged, assuming one starts from lattice scale interactions at high energies. This requires a systematic treatment of LL-mixing [87–89] coupled with a renormalization group approach [90, 91] involving all the couplings. We hope to address these and other important questions in the near future.

We acknowledge useful discussions with Mark Goerbig and Thierry Jolicoeur. J.A. is grateful to the University of Kentucky Center for Computational Sciences and Information Technology Services Research Computing for the use of the Morgan Compute Cluster. G.M. is grateful for the wonderful environment at the Aspen Center for Physics (NSF grant PHY-1607611). ACB and GM are grateful to the International Centre for Theoretical Sciences (ICTS) for supporting the program - Condensed Matter meets Quantum Information (code: ICTS/COMQUI2023/9), where parts of this project were conceived. Computational portions of this work were undertaken on the Nandadevi supercomputer, maintained and supported by the Institute of Mathematical Science's High-Performance Computing Center. Some of the numerical calculations were performed using the DiagHam libraries [92]. ACB thanks the Science and Engineering Research Board (SERB) of the Department of Science and Technology (DST) for funding support via the Mathematical Research Impact Centric Support (MATRICS) Grant No. MTR/2023/000002.

* Jincheng.An@uky.edu

† cb.ajit@gmail.com

‡ murthy@g.uky.edu

- [1] K. v. Klitzing, G. Dorda, and M. Pepper, New method for high-accuracy determination of the fine-structure constant based on quantized Hall resistance, *Phys. Rev. Lett.* **45**, 494 (1980).
- [2] D. J. Thouless, M. Kohmoto, M. P. Nightingale, and M. den Nijs, Quantized Hall conductance in a two-dimensional periodic potential, *Phys. Rev. Lett.* **49**, 405 (1982).
- [3] D. C. Tsui, H. L. Stormer, and A. C. Gossard, Two-dimensional magnetotransport in the extreme quantum limit, *Phys. Rev. Lett.* **48**, 1559 (1982).
- [4] R. B. Laughlin, Anomalous quantum Hall effect: An incompressible quantum fluid with fractionally charged excitations, *Phys. Rev. Lett.* **50**, 1395 (1983).
- [5] R. Prange and S. M. Girvin, *The Quantum Hall Effect* (Springer Verlag, 1990).
- [6] S. Das Sarma and A. Pinczuk, eds., *Perspectives in Quantum Hall Effects* (Wiley, 1996).
- [7] C. L. Kane and E. J. Mele, Z_2 topological order and the quantum spin Hall effect, *Phys. Rev. Lett.* **95**, 146802 (2005).
- [8] M. Z. Hasan and C. L. Kane, Colloquium: Topological insulators, *Rev. Mod. Phys.* **82**, 3045 (2010).
- [9] B. I. Halperin, Quantized Hall conductance, current-carrying edge states, and the existence of extended states in a two-dimensional disordered potential, *Phys. Rev. B* **25**, 2185 (1982).
- [10] H. A. Fertig, Energy spectrum of a layered system in a strong magnetic field, *Phys. Rev. B* **40**, 1087 (1989).
- [11] S. L. Sondhi, A. Karlhede, S. A. Kivelson, and E. H. Rezayi, Skyrmions and the crossover from the integer to fractional quantum Hall effect at small Zeeman energies, *Phys. Rev. B* **47**, 16419 (1993).
- [12] K. Yang, K. Moon, L. Zheng, A. H. MacDonald, S. M. Girvin, D. Yoshioka, and S.-C. Zhang, Quantum ferromagnetism and phase transitions in double-layer quantum Hall systems, *Phys. Rev. Lett.* **72**, 732 (1994).
- [13] K. Moon, H. Mori, K. Yang, S. M. Girvin, A. H. MacDonald, L. Zheng, D. Yoshioka, and S.-C. Zhang, Spontaneous interlayer coherence in double-layer quantum Hall systems: Charged vortices and Kosterlitz-Thouless phase transitions, *Phys. Rev. B* **51**, 5138 (1995).
- [14] C. Berger, Z. Song, T. Li, X. Li, A. Y. Ogbazghi, R. Feng, Z. Dai, A. N. Marchenkov, E. H. Conrad, P. N. First, and W. A. de Heer, Ultrathin epitaxial graphite: 2d electron gas properties and a route toward graphene-based nanoelectronics, *The Journal of Physical Chemistry B* **108**, 19912 (2004).
- [15] K. S. Novoselov, A. K. Geim, S. V. Morozov, D. Jiang, Y. Zhang, S. V. Dubonos, I. V. Grigorieva, and A. A. Firsov, Electric field effect in atomically thin carbon films, *Science* **306**, 666 (2004), <https://www.science.org/doi/pdf/10.1126/science.1102896>.
- [16] Y. Zhang, J. P. Small, M. E. S. Amori, and P. Kim, Electric field modulation of galvanomagnetic properties of mesoscopic graphite, *Phys. Rev. Lett.* **94**, 176803 (2005).
- [17] Z. Jiang, Y. Zhang, H. L. Stormer, and P. Kim, Quantum Hall states near the charge-neutral Dirac point in graphene, *Phys. Rev. Lett.* **99**, 106802 (2007).
- [18] A. H. Castro Neto, F. Guinea, N. M. R. Peres, K. S. Novoselov, and A. K. Geim, The electronic properties of graphene, *Rev. Mod. Phys.* **81**, 109 (2009).
- [19] A. F. Young, C. R. Dean, L. Wang, H. Ren, P. Cadden-Zimansky, K. Watanabe, T. Taniguchi, J. Hone, K. L. Shepard, and P. Kim, Spin and valley quantum Hall ferromagnetism in graphene, *Nature Physics* **8**, 550–556 (2012).
- [20] P. Maher, C. R. Dean, A. F. Young, T. Taniguchi, K. Watanabe, K. L. Shepard, J. Hone, and P. Kim, Evidence for a spin phase transition at charge neutrality in bilayer graphene, *Nature Physics* **9**, 154–158 (2013).
- [21] A. F. Young, J. D. Sanchez-Yamagishi, B. Hunt, S. H. Choi, K. Watanabe, T. Taniguchi, R. C. Ashoori, and P. Jarillo-Herrero, Tunable symmetry breaking and helical edge transport in a graphene quantum spin Hall state, *Nature* **505**, 528 (2014).
- [22] D. S. Wei, T. van der Sar, S. H. Lee, K. Watanabe, T. Taniguchi, B. I. Halperin, and A. Yacoby, Electrical generation and detection of spin waves in a quantum Hall ferromagnet, *Science* **362**, 229–233 (2018).
- [23] P. Stepanov, S. Che, D. Shcherbakov, J. Yang, R. Chen, K. Thilakar, G. Voigt, M. W. Bockrath, D. Smirnov, K. Watanabe, T. Taniguchi, R. K. Lake, Y. Barlas, A. H. MacDonald, and C. N. Lau, Long-distance spin transport through a graphene quantum Hall antiferromagnet, *Nature Physics* **14**, 907 (2018).
- [24] A. Assouline, M. Jo, P. Brasseur, K. Watanabe, T. Taniguchi, T. Jolicoeur, D. C. Glattli, N. Kumada, P. Roche, F. D. Parmentier, and et al., Excitonic nature of magnons in a quantum Hall ferromagnet, *Nature*

- Physics* **17**, 1369–1374 (2021).
- [25] H. Zhou, C. Huang, N. Wei, T. Taniguchi, K. Watanabe, M. P. Zaletel, Z. Papić, A. H. MacDonald, and A. F. Young, Strong-magnetic-field magnon transport in monolayer graphene, *Physical Review X* **12**, 10.1103/physrevx.12.021060 (2022).
- [26] S.-Y. Li, Y. Zhang, L.-J. Yin, and L. He, Scanning tunneling microscope study of quantum Hall isospin ferromagnetic states in the zero Landau level in a graphene monolayer, *Phys. Rev. B* **100**, 085437 (2019).
- [27] X. Liu, G. Farahi, C.-L. Chiu, Z. Papic, K. Watanabe, T. Taniguchi, M. P. Zaletel, and A. Yazdani, Visualizing broken symmetry and topological defects in a quantum Hall ferromagnet, *Science* **375**, 321–326 (2022).
- [28] A. Coissard, D. Wander, H. Vignaud, A. G. Grushin, C. Repellin, K. Watanabe, T. Taniguchi, F. Gay, C. B. Winkelmann, H. Courtois, H. Sellier, and B. Sacépé, Imaging tunable quantum Hall broken-symmetry orders in graphene, *Nature* **605**, 51 (2022).
- [29] X. Du, I. Skachko, F. Duerr, A. Luican, and E. Y. Andrei, Fractional quantum Hall effect and insulating phase of Dirac electrons in graphene, *Nature* **462**, 192 (2009).
- [30] K. Bolotin, F. Ghahari, M. D. Shulman, H. Stormer, and P. Kim, Observation of the fractional quantum Hall effect in graphene, *Nature* **462**, 196 (2009).
- [31] C. R. Dean, A. F. Young, P. Cadden-Zimansky, L. Wang, H. Ren, K. Watanabe, T. Taniguchi, P. Kim, J. Hone, and K. L. Shepard, Multicomponent fractional quantum Hall effect in graphene, *Nature Physics* **7**, 693 (2011).
- [32] B. Hunt, J. D. Sanchez-Yamagishi, A. F. Young, M. Yankowitz, B. J. LeRoy, K. Watanabe, T. Taniguchi, P. Moon, M. Koshino, P. Jarillo-Herrero, and R. C. Ashoori, Massive Dirac fermions and Hofstadter butterfly in a van der Waals heterostructure, *Science* **340**, 1427 (2013), <http://science.sciencemag.org/content/340/6139/1427.full.pdf>
- [33] F. Amet, A. J. Bestwick, J. R. Williams, L. Balicas, K. Watanabe, T. Taniguchi, and D. Goldhaber-Gordon, Composite fermions and broken symmetries in graphene, *Nat. Commun.* **6**, 5838 (2015).
- [34] A. A. Zibrov, E. M. Spanton, H. Zhou, C. Kometter, T. Taniguchi, K. Watanabe, and A. F. Young, Even-denominator fractional quantum Hall states at an isospin transition in monolayer graphene, *Nature Physics* **14**, 930 (2018).
- [35] H. Zhou, H. Polshyn, T. Taniguchi, K. Watanabe, and A. F. Young, Solids of quantum Hall skyrmions in graphene, *Nature Physics* **16**, 154–158 (2019).
- [36] K. Huang, H. Fu, D. R. Hickey, N. Alem, X. Lin, K. Watanabe, T. Taniguchi, and J. Zhu, Valley isospin controlled fractional quantum Hall states in bilayer graphene, *Phys. Rev. X* **12**, 031019 (2022).
- [37] J. Alicea and M. P. A. Fisher, Graphene integer quantum Hall effect in the ferromagnetic and paramagnetic regimes, *Phys. Rev. B* **74**, 075422 (2006).
- [38] K. Yang, S. Das Sarma, and A. H. MacDonald, Collective modes and skyrmion excitations in graphene $SU(4)$ quantum Hall ferromagnets, *Phys. Rev. B* **74**, 075423 (2006).
- [39] I. F. Herbut, Theory of integer quantum Hall effect in graphene, *Phys. Rev. B* **75**, 165411 (2007).
- [40] I. F. Herbut, $SO(3)$ symmetry between Néel and ferromagnetic order parameters for graphene in a magnetic field, *Phys. Rev. B* **76**, 085432 (2007).
- [41] D. A. Abanin, P. A. Lee, and L. S. Levitov, Spin-filtered edge states and quantum Hall effect in graphene, *Phys. Rev. Lett.* **96**, 176803 (2006).
- [42] H. A. Fertig and L. Brey, Luttinger liquid at the edge of undoped graphene in a strong magnetic field, *Phys. Rev. Lett.* **97**, 116805 (2006).
- [43] M. Kharitonov, Phase diagram for the $\nu = 0$ quantum Hall state in monolayer graphene, *Phys. Rev. B* **85**, 155439 (2012).
- [44] G. Farahi, C.-L. Chiu, X. Liu, Z. Papic, K. Watanabe, T. Taniguchi, M. P. Zaletel, and A. Yazdani, Broken symmetries and excitation spectra of interacting electrons in partially filled Landau levels (2023), [arXiv:2303.16993](https://arxiv.org/abs/2303.16993) [cond-mat.mes-Hall].
- [45] Y. Hu, Y.-C. Tsui, M. He, U. Kamber, T. Wang, A. S. Mohammadi, K. Watanabe, T. Taniguchi, Z. Papić, M. P. Zaletel, and A. Yazdani, High-resolution tunneling spectroscopy of fractional quantum Hall states (2023), [arXiv:2308.05789](https://arxiv.org/abs/2308.05789) [cond-mat.mes-Hall].
- [46] A. Das, R. K. Kaul, and G. Murthy, Coexistence of canted antiferromagnetism and bond order in $\nu = 0$ graphene, *Phys. Rev. Lett.* **128**, 106803 (2022).
- [47] S. J. De, A. Das, S. Rao, R. K. Kaul, and G. Murthy, Global phase diagram of charge-neutral graphene in the quantum Hall regime for generic interactions, *Phys. Rev. B* **107**, 125422 (2023).
- [48] N. Stefanidis and I. S. Villadiego, Spin-valley entangled quantum Hall states in graphene, *Phys. Rev. B* **108**, 235137 (2023).
- [49] I. Sodemann and A. H. MacDonald, Broken $SU(4)$ symmetry and the fractional quantum Hall effect in graphene, *Phys. Rev. Lett.* **112**, 126804 (2014).
- [50] F. D. M. Haldane, Fractional quantization of the Hall effect: A hierarchy of incompressible quantum fluid states, *Phys. Rev. Lett.* **51**, 605 (1983).
- [51] S. S. Hegde and I. S. Villadiego, Theory of competing charge density wave, Kekulé, and antiferromagnetically ordered fractional quantum Hall states in graphene aligned with boron nitride, *Phys. Rev. B* **105**, 195417 (2022).
- [52] R. K. Dora and A. C. Balram, Competition between fractional quantum Hall liquid and electron solid phases in the Landau levels of multilayer graphene, *Phys. Rev. B* **108**, 235153 (2023).
- [53] G. Murthy, E. Shimshoni, and H. A. Fertig, Spin-valley coherent phases of the $\nu = 0$ quantum Hall state in bilayer graphene, *Phys. Rev. B* **96**, 245125 (2017).
- [54] U. Khanna, K. Huang, G. Murthy, H. A. Fertig, K. Watanabe, T. Taniguchi, J. Zhu, and E. Shimshoni, Phase diagram of the $\nu = 2$ quantum hall state in bilayer graphene, *Phys. Rev. B* **108**, L041107 (2023).
- [55] N. Stefanidis and I. S. Villadiego, Competing spin-valley entangled and broken symmetry states in the $n = 1$ Landau level of graphene, *Phys. Rev. B* **107**, 045132 (2023).
- [56] Y. Lian, A. Rosch, and M. O. Goerbig, $SU(4)$ skyrmions in the $\nu = \pm 1$ quantum Hall state of graphene, *Phys. Rev. Lett.* **117**, 056806 (2016).
- [57] Y. Lian and M. O. Goerbig, Spin-valley skyrmions in graphene at filling factor $\nu = -1$, *Phys. Rev. B* **95**, 245428 (2017).
- [58] J. Atteia and M. O. Goerbig, $SU(4)$ spin waves in the $\nu = \pm 1$ quantum Hall ferromagnet in graphene, *Phys. Rev. B* **103**, 195413 (2021).
- [59] F. Amet, J. R. Williams, K. Watanabe, T. Taniguchi, and

- D. Goldhaber-Gordon, Insulating behavior at the neutrality point in single-layer graphene, *Phys. Rev. Lett.* **110**, 216601 (2013).
- [60] B. Hunt, J. D. Sanchez-Yamagishi, A. F. Young, M. Yankowitz, B. J. LeRoy, K. Watanabe, T. Taniguchi, P. Moon, M. Koshino, P. Jarillo-Herrero, and R. C. Ashoori, Massive Dirac fermions and Hofstadter butterfly in a van der Waals heterostructure, *Science* **340**, 1427 (2013).
- [61] J. Jung, A. M. DaSilva, A. H. MacDonald, and S. Adam, Origin of band gaps in graphene on hexagonal boron nitride, *Nature Communications* **6**, 6308 (2015).
- [62] J. Jung, E. Laksono, A. M. DaSilva, A. H. MacDonald, M. Mucha-Kruczyński, and S. Adam, Moiré band model and band gaps of graphene on hexagonal boron nitride, *Phys. Rev. B* **96**, 085442 (2017).
- [63] See Supplemental Material for details on the spinors, phase diagrams at nonzero E_v , the structure of the ansatz for three-component states, phase diagrams for $\nu = -2+2/3$, and phase diagrams at $-2+5/3$ including the Coulomb interaction.
- [64] Z. Papić, M. O. Goerbig, and N. Regnault, Atypical fractional quantum Hall effect in graphene at filling factor $1/3$, *Phys. Rev. Lett.* **105**, 176802 (2010).
- [65] F. Wu, I. Sodemann, Y. Araki, A. H. MacDonald, and T. Jolicoeur, $SO(5)$ symmetry in the quantum Hall effect in graphene, *Phys. Rev. B* **90**, 235432 (2014).
- [66] F. Wu, I. Sodemann, A. H. MacDonald, and T. Jolicoeur, $SU(3)$ and $SU(4)$ singlet quantum Hall states at $\nu = 2/3$, *Phys. Rev. Lett.* **115**, 166805 (2015).
- [67] N. D. Le and T. Jolicoeur, Spin and valley ordering of fractional quantum Hall states in monolayer graphene, *Phys. Rev. B* **105**, 075203 (2022).
- [68] B. Douçot, M. O. Goerbig, P. Lederer, and R. Moessner, Entanglement skyrmions in multicomponent quantum Hall systems, *Phys. Rev. B* **78**, 195327 (2008).
- [69] J. Atteia, Y. Lian, and M. O. Goerbig, Skyrmion zoo in graphene at charge neutrality in a strong magnetic field, *Phys. Rev. B* **103**, 035403 (2021).
- [70] J. K. Jain, Composite-fermion approach for the fractional quantum Hall effect, *Phys. Rev. Lett.* **63**, 199 (1989).
- [71] A. C. Balram, C. Töke, A. Wójs, and J. K. Jain, Phase diagram of fractional quantum Hall effect of composite fermions in multicomponent systems, *Phys. Rev. B* **91**, 045109 (2015).
- [72] N. d’Ambrumenil and A. M. Reynolds, Fractional quantum Hall states in higher Landau levels, *Journal of Physics C: Solid State Physics* **21**, 119 (1988).
- [73] G. Dev and J. K. Jain, Jastrow-Slater trial wave functions for the fractional quantum Hall effect: Results for few-particle systems, *Phys. Rev. B* **45**, 1223 (1992).
- [74] X. G. Wu, G. Dev, and J. K. Jain, Mixed-spin incompressible states in the fractional quantum Hall effect, *Phys. Rev. Lett.* **71**, 153 (1993).
- [75] J. K. Jain, *Composite Fermions* (Cambridge University Press, New York, US, 2007).
- [76] B. Yang and A. C. Balram, Elementary excitations in fractional quantum Hall effect from classical constraints, *New Journal of Physics* **23**, 013001 (2021).
- [77] A. C. Balram and A. Wójs, Fractional quantum Hall effect at $\nu = 2+4/9$, *Phys. Rev. Research* **2**, 032035 (2020).
- [78] A. C. Balram, Transitions from Abelian composite fermion to non-Abelian parton fractional quantum Hall states in the zeroth Landau level of bilayer graphene, *Phys. Rev. B* **105**, L121406 (2022).
- [79] A. C. Balram and J. K. Jain, Nature of composite fermions and the role of particle-hole symmetry: A microscopic account, *Phys. Rev. B* **93**, 235152 (2016).
- [80] A. C. Balram, C. Töke, A. Wójs, and J. K. Jain, Fractional quantum Hall effect in graphene: Quantitative comparison between theory and experiment, *Phys. Rev. B* **92**, 075410 (2015).
- [81] W. N. Faugno, A. C. Balram, A. Wójs, and J. K. Jain, Theoretical phase diagram of two-component composite fermions in double-layer graphene, *Phys. Rev. B* **101**, 085412 (2020).
- [82] G. Li, A. Luican, and E. Y. Andrei, Scanning tunneling spectroscopy of graphene on graphite, *Phys. Rev. Lett.* **102**, 176804 (2009).
- [83] H. Fu, K. Huang, K. Watanabe, T. Taniguchi, and J. Zhu, Gapless spin wave transport through a quantum canted antiferromagnet, *Phys. Rev. X* **11**, 021012 (2021).
- [84] B. E. Feldman, A. J. Levin, B. Krauss, D. A. Abanin, B. I. Halperin, J. H. Smet, and A. Yacoby, Fractional quantum Hall phase transitions and four-flux states in graphene, *Phys. Rev. Lett.* **111**, 076802 (2013).
- [85] Y. Kim, A. C. Balram, T. Taniguchi, K. Watanabe, J. K. Jain, and J. H. Smet, Even denominator fractional quantum Hall states in higher Landau levels of graphene, *Nature Physics* **15**, 154 (2019).
- [86] Work in progress.
- [87] G. Murthy and R. Shankar, Hamiltonian theory of the fractional quantum Hall effect: Effect of Landau level mixing, *Phys. Rev. B* **65**, 245309 (2002).
- [88] M. R. Peterson and C. Nayak, More realistic Hamiltonians for the fractional quantum Hall regime in GaAs and graphene, *Phys. Rev. B* **87**, 245129 (2013).
- [89] M. R. Peterson and C. Nayak, Effects of Landau level mixing on the fractional quantum Hall effect in monolayer graphene, *Phys. Rev. Lett.* **113**, 086401 (2014).
- [90] O. Vafek and J. Kang, Renormalization group study of hidden symmetry in twisted bilayer graphene with Coulomb interactions, *Phys. Rev. Lett.* **125**, 257602 (2020).
- [91] W. Qin, C. Huang, T. Wolf, N. Wei, I. Blinov, and A. H. MacDonald, Functional renormalization group study of superconductivity in rhombohedral trilayer graphene, *Phys. Rev. Lett.* **130**, 146001 (2023).
- [92] DiagHam, <https://www.nick-ux.org/diagham>.

Supplemental Material for “Magnetic and Lattice Ordered Fractional Quantum Hall Phases in Graphene”

Jincheng An,^{1,*} Ajit C. Balram^{2,3,†} and Ganpathy Murthy^{1,‡}

¹*Department of Physics and Astronomy, University of Kentucky, Lexington, KY 40506, USA*

²*Institute of Mathematical Sciences, CIT Campus, Chennai, 600113, India*

³*Homi Bhabha National Institute, Training School Complex, Anushaktinagar, Mumbai 400094, India*

This supplemental material contains many technical details about the results presented in the main text. In Sec. **SI** we briefly review the Haldane pseudopotentials and the matrix elements of the two-body interactions restricted to relative angular momentum $m=0, 1$. In Sec. **SII** we present the rationale behind the structure of the spinors we have chosen. The calculation of the variational energy for general fillings is presented in Sec. **SIII**. In Sec. **SIV** we present the details of the phases shown in the main text for the state $(1, [2, 0]_{-2}, 0) \equiv (1, 2/3, 0, 0)$. Since we focused on the valley symmetric situation ($E_v=0$) in the main text, we also present some phase diagrams showing the evolution with E_v . In Sec. **SV** we do the same for the state $(1, [1, 1]_{-2}, 0) \equiv (1, 1/3, 1/3, 0)$. Finally, we consider the Coulomb interaction as well, taking into account the Coulomb energy difference between the two-component states (2CS) and three-component states (3CS), and show a few phase diagrams that manifest transitions between the 2CS and 3CS in Sec. **SVI**.

SI. HALDANE PSEUDOPOTENTIALS

The Haldane pseudopotentials [1] is a compact way of parameterizing any two-body interaction that is translationally and rotationally invariant, projected to a single Landau level. The key idea is that such an interaction depends only on the magnitude of the relative coordinate between two particles and therefore can be expanded in the basis of the center of mass angular momentum M and the relative angular momentum m . The four-fermion interaction matrix element in the symmetric gauge can be written as

$$V_{m_1 m_2 m_3 m_4} = \langle m_1, m_2 | \hat{V} | m_3, m_4 \rangle = \sum_m V_m \sum_M \langle m_1, m_2 | M, m \rangle \langle M, m | m_3, m_4 \rangle, \quad (\text{S1})$$

where the V_m are the Haldane pseudopotentials [1]. Since we keep only V_0 and V_1 , we need

$$\langle m_1, m_2 | m_1 + m_2, 0 \rangle = \frac{1}{\sqrt{2^{m_1+m_2}}} \sqrt{\frac{(m_1+m_2)!}{m_1! m_2!}}, \quad \langle m_1, m_2 | m_1 + m_2 - 1, 1 \rangle = \frac{m_1 - m_2}{\sqrt{2^{m_1+m_2}}} \sqrt{\frac{(m_1+m_2-1)!}{m_1! m_2!}}. \quad (\text{S2})$$

If one carries a Hartree-Fock (HF) approximation on a state with well-defined total angular momentum,

$$\begin{aligned} (V_0^H)_{m_1 m_2} &= (V_0)_{m_1 m_2 m_2 m_1} = (V_0)_{m_1 m_2 m_1 m_2} = (V_0^F)_{m_1 m_2}, \\ (V_1^H)_{m_1 m_2} &= (V_1)_{m_1 m_2 m_2 m_1} = -(V_1)_{m_1 m_2 m_1 m_2} = -(V_1^F)_{m_1 m_2}, \end{aligned} \quad (\text{S3})$$

the Hartree coupling will be identical to the Fock coupling for \hat{V}_0 while their sign will be opposite for \hat{V}_1 . For future convenience, we define two sums that appear repeatedly in the energy functional and happen to both be equal to 2.

$$S_0 = \frac{1}{N_\phi} \sum_{m_1 m_2} (V_0)_{m_1 m_2 m_2 m_1} = S_1 = \frac{1}{N_\phi} \sum_{m_1 m_2} (V_1)_{m_1 m_2 m_2 m_1} = 2. \quad (\text{S4})$$

SII. SPINOR ANSATZ FOR VARIATION

Our ansatz for the spinors is a generalization of ansatzes that have been used in the literature [2–7]. We begin with some general considerations. We use the $U(1)_s \otimes U(1)_v$ symmetry of the Hamiltonian to make all the spinors real, which means that they all live on the three-sphere S^3 . To see what this restriction means, let us consider a product

* Jincheng.An@uky.edu

† cb.ajit@gmail.com

‡ murthy@g.uky.edu

spinor $|\mathbf{n}, \mathbf{s}\rangle = |\mathbf{n}\rangle \otimes |\mathbf{s}\rangle$, where $|\mathbf{n}\rangle = [\cos(\theta_n/2), e^{i\phi_n} \sin(\theta_n/2)]^T$, $|\mathbf{s}\rangle = [\cos(\theta_s/2), e^{i\phi_s} \sin(\theta_s/2)]^T$. The imaginary parts appear via the projection of \mathbf{n} or \mathbf{s} in their respective xy -planes. So we assume that if the occupied spinors have nontrivial projections in the spin xy -plane, say, they will all align so that a single $U(1)_s \otimes U(1)_v$ rotation will make them real. One spinor can thus be described by three angles. Two orthogonal spinors need five angles (three for each spinor, with one orthogonality constraint), and three need six angles to describe. We also need ansatzes that can describe states where each spinor can have a different spin direction or a different valley direction. Thus, we start with the following ansatz

$$\begin{aligned} |f_1\rangle &= \cos(\alpha_1/2)|\mathbf{n}, \mathbf{s}_a\rangle + \sin(\alpha_1/2)|-\mathbf{n}, -\mathbf{s}_b\rangle, & |f_2\rangle &= \cos(\alpha_2/2)|\mathbf{n}, -\mathbf{s}_a\rangle + \sin(\alpha_2/2)|-\mathbf{n}, \mathbf{s}_b\rangle, \\ |f_3\rangle &= \sin(\alpha_1/2)|\mathbf{n}, \mathbf{s}_a\rangle - \cos(\alpha_1/2)|-\mathbf{n}, -\mathbf{s}_b\rangle, & |f_4\rangle &= \sin(\alpha_2/2)|\mathbf{n}, -\mathbf{s}_a\rangle - \cos(\alpha_2/2)|-\mathbf{n}, \mathbf{s}_b\rangle. \end{aligned} \quad (\text{S5})$$

We use the $U(1)_s \otimes U(1)_v$ symmetry to restrict the azimuthal angles ϕ_i to be either 0 or π . One can see that the description of $|f_i\rangle$ requires only five continuously varying angles, namely $\alpha_1, \alpha_2, \theta_n, \theta_a, \theta_b$. Thus, this ansatz will be sufficient to describe two orthogonal spinors but is not general enough to describe three orthogonal spinors by our earlier counting argument. Hence, in describing states such as $(1, [1, 1]_{-2}, 0) \equiv (1, 1/3, 1/3, 0)$, where three orthogonal spinors are necessarily involved, we make a further set of rotations by introducing two more angles η_1, η_2 as shown below.

$$\begin{aligned} |\tilde{f}_1\rangle &= \cos(\eta_1/2)|f_1\rangle + \sin(\eta_1/2)|f_2\rangle, & |\tilde{f}_2\rangle &= -\sin(\eta_1/2)|f_1\rangle + \cos(\eta_1/2)|f_2\rangle, \\ |\tilde{f}_3\rangle &= \cos(\eta_2/2)|f_3\rangle + \sin(\eta_2/2)|f_4\rangle, & |\tilde{f}_4\rangle &= -\sin(\eta_2/2)|f_3\rangle + \cos(\eta_2/2)|f_4\rangle, \end{aligned} \quad (\text{S6})$$

Our description now uses seven continuously varying angles and is therefore slightly redundant. However, we believe it is complete. We have found through experience that the first ansatz, Eq. (S5), misses certain phases for the state $(1, [1, 1]_{-2}, 0)$ with fillings $(1, 1/3, 1/3, 0)$, while the second sufficient but redundant ansatz, Eq. (S6), does capture them.

For $\vec{\nu} = (\nu_1, \nu_2, \dots)$, all order parameters \hat{O} 's mentioned in this work are computed as $\langle \hat{O} \rangle = \sum_i \nu_i \text{Tr}(P_i \hat{O}) / \sum_i \nu_i$, where $P_i = |f_i\rangle \langle f_i|$ is the project onto the state $|f_i\rangle$. Phases are differentiated by numerically determining whether various order parameters $\langle \hat{O} \rangle$'s are zero or not.

III. VARIATIONAL ENERGY

With guiding center index sums being implicit, the residual anisotropic interaction we consider, which has support only in the relative angular momentum $m=0, 1$ channels, can be written as

$$\begin{aligned} \hat{H}^{\text{an}} &\propto g_{\perp} : \hat{\tau}^x \hat{\tau}^x + \hat{\tau}^y \hat{\tau}^y : + g_z : \hat{\tau}^z \hat{\tau}^z :, \\ g_{\perp} &= g_{0,\perp} + g_{1,\perp}, \quad g_z = g_{0,z} + g_{1,z}, \quad \hat{\tau}^i = c_{\alpha}^{\dagger} \tau_{\alpha\beta}^i c_{\beta}. \end{aligned} \quad (\text{S7})$$

Due to Eq. (S3), $g_{0,\perp}^H = g_{0,\perp}^F$, $g_{1,\perp}^H = -g_{1,\perp}^F$; $g_{0,z}^H = g_{0,z}^F$, $g_{1,z}^H = -g_{1,z}^F$. We will parameterize the non-USR nature of the interactions using the differences between Hartree and Fock couplings by $\Delta_{\perp} = g_{\perp}^H - g_{\perp}^F = 2g_{1,\perp}$, $\Delta_z = g_z^H - g_z^F = 2g_{1,z}$. The Hamiltonian for the residual anisotropic interactions written out in full is

$$\hat{H}^{\text{an}} = \frac{1}{2} \sum_{\{m_i\}, \alpha\beta\gamma\delta} V_{m_1 m_2 m_3 m_4}^{\alpha\beta\gamma\delta} c_{m_1\alpha}^{\dagger} c_{m_2\beta}^{\dagger} c_{m_3\gamma} c_{m_4\delta}. \quad (\text{S8})$$

It is crucial that the matrix elements have a product structure, with a part that depends only on the guiding center indices m_i multiplied by a part that depends on the spin-valley indices $\alpha\beta\gamma\delta$. Explicitly,

$$\begin{aligned} V_{m_1 m_2 m_3 m_4}^{\alpha\beta\gamma\delta} &= \mathcal{T}_{\alpha\delta}^z \mathcal{T}_{\beta\gamma}^z \left(g_{0,z}(V_0)_{m_1 m_2 m_3 m_4} + g_{1,z}(V_1)_{m_1 m_2 m_3 m_4} \right) \\ &+ \left(\mathcal{T}_{\alpha\delta}^x \mathcal{T}_{\beta\gamma}^x + \mathcal{T}_{\alpha\delta}^y \mathcal{T}_{\beta\gamma}^y \right) \left(g_{0,\perp}(V_0)_{m_1 m_2 m_3 m_4} + g_{1,\perp}(V_1)_{m_1 m_2 m_3 m_4} \right), \end{aligned} \quad (\text{S9})$$

where \mathcal{T} are the 4×4 matrices in spin-valley space with the spin-part set to identity and the valley part being the 2×2 Pauli matrix τ . In computing the variational energy, since the initial and final states are identical, either all four Fermi operators operate on the same spinor, or a creation-destruction pair acts on one spinor, while the other creation-destruction pair acts on another spinor [3]. When at least two of the fermion operators belong to a fully

occupied spinor we can make a further simplification, that of replacing the average of the product of four fermion operators by the product of averages of $\langle c^\dagger c \rangle$.

$$\begin{aligned} \langle \hat{H}^{\text{an}} \rangle &= \frac{N_\phi}{2} \sum_{m=0,1} \nu_1 \nu_2 S_m \mathcal{E}^{\text{an}}(P_1, P_2, g_{m,\perp}, g_{m,z}) \\ \mathcal{E}^{\text{an}}(P_1, P_2, g_\perp, g_z) &= g_\perp^H (\text{Tr}(P_1 \tau_x) \text{Tr}(P_2 \tau_x) + \text{Tr}(P_1 \tau_y) \text{Tr}(P_2 \tau_y)) + g_z^H \text{Tr}(P_1 \tau_z) \text{Tr}(P_2 \tau_z) \\ &\quad - g_\perp^F (\text{Tr}(P_1 \tau_x P_2 \tau_x) + \text{Tr}(P_1 \tau_y P_2 \tau_y)) - g_z^F \text{Tr}(P_1 \tau_z P_2 \tau_z) \end{aligned} \quad (\text{S10})$$

First, we consider the variational energy when a certain number of spinors are fully filled, and one spinor is $2/3$ filled. We will label this as $(1^n, 2/3) \equiv |1f_1, \dots, 1f_n, (2/3)f_{n+1}\rangle$. It is convenient to define a separate projector ($P_I = \sum_{i=1}^n P_i$) for the fully filled levels. The variational energy of $(1^n, 2/3)$ is given by

$$\begin{aligned} E_{(1^n, \frac{2}{3})}^{\text{an}} &= \frac{1}{2} \sum_{m=0,1} S_m \mathcal{E}^{\text{an}}(P_I, P_I, g_{m,\perp}, g_{m,z}) + \frac{2}{3} \sum_{m=0,1} S_m \mathcal{E}^{\text{an}}(P_I, P_{n+1}, g_{m,\perp}, g_{m,z}) \\ &\quad + \frac{1}{2} \frac{\langle 2/3 | \hat{V}_1 | 2/3 \rangle}{2N_\phi} \mathcal{E}^{\text{an}}(P_{n+1}, P_{n+1}, g_{1,\perp}, g_{1,z}) - \text{Tr}(P(E_z \sigma_z + E_v \tau_z)). \end{aligned} \quad (\text{S11})$$

By an antiunitary particle-hole transformation [3] we obtain $\langle 2/3 | \hat{V}_1 | 2/3 \rangle = \langle 1 | \hat{V}_1 | 1 \rangle / 3$. Now we turn to the filling $(1^n, \frac{1}{3}, \frac{1}{3})$ where there are n integer filled spinors and two $\frac{1}{3}$ fractional filled spinors $|\Psi_{(1^n, 1/3, 1/3)}\rangle = |1f_1, \dots, 1f_n, (1/3)f_{n+1}, (1/3)f_{n+2}\rangle$. It is understood that the fractionally filled spinors are in the singlet state $(1, [1, 1]_{-2}, 0)$ as described in the main text, and are not a product of two $1/3$ Laughlin states. The energy functional is

$$\begin{aligned} E_{(1^n, \frac{1}{3}, \frac{1}{3})}^{\text{an}} &= \frac{1}{2} \sum_{m=0,1} S_m \mathcal{E}^{\text{an}}(P_I, P_I, g_{m,\perp}, g_{m,z}) + \frac{1}{3} \sum_{m=0,1} S_m \mathcal{E}^{\text{an}}(P_I, P_{n+1} + P_{n+2}, g_{m,\perp}, g_{m,z}) \\ &\quad + \frac{a}{4} \mathcal{E}^{\text{an}}(P_{n+1} + P_{n+2}, P_{n+1} + P_{n+2}, g_{1,\perp}, g_{1,z}) - \text{Tr}((P(E_z \sigma_z + E_v \tau_z))) \end{aligned} \quad (\text{S12})$$

The third term on the RHS, the interaction in the correlated fractionally filled spinors is derived as follows. We project to that two-dimensional (2D) subspace and write all matrices such as the τ^μ in that basis as $\tilde{\tau}_{ij}^\mu = \langle f_i | \tau^\mu | f_j \rangle$, with $i, j=1, 2$ representing the states $|f_{n+1}\rangle, |f_{n+2}\rangle$ respectively. Listing out these possibilities, specializing to the $m=1$ angular momentum channel, and using antisymmetry we obtain

$$\begin{aligned} &\langle \Psi | \frac{1}{2} \sum_{\{m_i\} j_1 j_2 j_3 j_4} g_\mu V_{m_1 m_2 m_3 m_4} \tilde{\tau}_{j_1 j_4}^\mu \tilde{\tau}_{j_2 j_3}^\mu c_{j_1 m_1}^\dagger c_{j_2 m_2}^\dagger c_{j_3 m_3} c_{j_4 m_4} | \Psi \rangle \\ &= \frac{g_\mu}{2} \sum_{\{m_i\}} (V_1)_{m_1 m_2 m_3 m_4} \left(\tilde{\tau}_{11}^\mu \tilde{\tau}_{11}^\mu \langle \Psi | c_{1 m_1}^\dagger c_{1 m_2}^\dagger c_{1 m_3} c_{1 m_4} | \Psi \rangle + \tilde{\tau}_{22}^\mu \tilde{\tau}_{22}^\mu \langle \Psi | c_{2 m_1}^\dagger c_{2 m_2}^\dagger c_{2 m_3} c_{2 m_4} | \Psi \rangle \right. \\ &\quad \left. + 2(\tilde{\tau}_{11}^\mu \tilde{\tau}_{22}^\mu + \tilde{\tau}_{12}^\mu \tilde{\tau}_{21}^\mu) \langle \Psi | c_{1 m_1}^\dagger c_{2 m_2}^\dagger c_{2 m_3} c_{1 m_4} | \Psi \rangle \right). \end{aligned} \quad (\text{S13})$$

One can no longer claim that (m_3, m_4) is a permutation of (m_1, m_2) because the state is strongly correlated. The averages have to be computed by exact diagonalization on the $[1, 1]_{-2}$ singlet state. Leaving all the m sums implicit, the result is the following:

$$(1/N_\phi) \langle \Psi | V_1 c_1^\dagger c_1^\dagger c_1 c_1 | \Psi \rangle = (1/N_\phi) \langle \Psi | V_1 c_2^\dagger c_2^\dagger c_2 c_2 | \Psi \rangle = (2/N_\phi) \langle \Psi | V_1 c_1^\dagger c_2^\dagger c_2 c_1 | \Psi \rangle = a. \quad (\text{S14})$$

Once we have Eqs. (S14), we notice that Eq. (S13) reduces to the third term of Eq. (S12). To find the number a , we carried out an exact diagonalization on finite systems on the sphere for the singlet $2/3$ state, with the Hamiltonian simply being the bare Coulomb interaction. The results for the singlet $2/3$ state are presented below for up to 14 electrons. Extrapolating to the thermodynamic limit we obtain $a=0.164$

Furthermore, it is found that $\langle V_0 \rangle \ll \langle V_1 \rangle$ (by three orders of magnitude). Therefore, in our calculations we set the average $\langle \frac{1}{3}, \frac{1}{3} | \hat{V}_0 | \frac{1}{3}, \frac{1}{3} \rangle$ to zero. Since the singlet state has a $U(2)$ symmetry of rotations within the 2D space spanned by the two spinors $|f_{n+1}\rangle, |f_{n+2}\rangle$. Thus, the contribution to the energy functional from this subspace must depend only on $P_1 + P_2$, as is verified in Eq. (S12).

In the next sections, we will present phase diagrams for $(1, 2/3, 0, 0)$ and $(1, 1/3, 1/3, 0)$. However, we would like to point out that the phase diagram for $(2/3, 0, 0, 0)$ is identical to that of $(1, 0, 0, 0)$ found in Ref. [5, 7], and that the phase diagram of $(1/3, 1/3, 0, 0)$ is identical to that of $(1, 1, 0, 0)$ found in Ref. [8], for a specific choice of parameters. We will explore these phase diagrams in detail in a forthcoming publication [9]

N_ϕ	N	$\langle V_0 \rangle$	$\langle V_1 \rangle$	$\langle V_0/N \rangle$	$\langle V_1/N \rangle$
5	4	0.0007	1.4859	0.0002	0.3715
8	6	0.0023	2.9583	0.0004	0.4931
11	8	0.0042	4.4245	0.0005	0.5531
14	10	0.0064	5.9104	0.0006	0.5910
17	12	0.0089	7.3871	0.0007	0.6156
20	14	0.0115	8.8622	0.0008	0.6330

TABLE S1: The pair-amplitudes in relative angular momentum $m=0,1$ for the exact $\nu=2/3$ spin-singlet Coulomb ground state obtained using exact diagonalization in the spherical geometry for N electrons at flux $N_\phi=3N/2-1$.

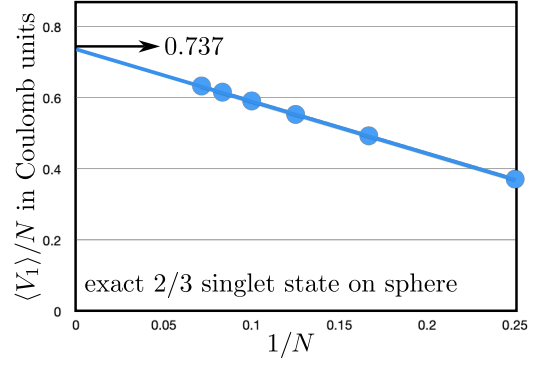


FIG. S1: Thermodynamic extrapolation of the pair-amplitude in relative angular momentum $m=1$ for the $2/3$ spin-singlet Coulomb ground state from finite system results in the spherical geometry.

SIV. PHASE DIAGRAMS FOR $(1, [2, 0]_{-2}, 0) \equiv (1, \frac{2}{3}, 0, 0)$

Let us briefly consider the USR limit, which was examined variationally at $E_v=0$ by Sodemann and MacDonald [3]. They found five phases: FM : $|K, \uparrow\rangle, |K', \uparrow\rangle$, CDW : $|K, \uparrow\rangle, |K, \downarrow\rangle$, BO : $|\hat{e}_x, \uparrow\rangle, |\hat{e}_x, \downarrow\rangle$, AF : $|K, \uparrow\rangle, |K', \downarrow\rangle$, CAF : $|K, \mathbf{s}_a\rangle, |K', \mathbf{s}_b\rangle$. In addition to these phases, we find an additional spin-valley entangled phase at $E_v=0$ as shown in Fig. S3a, which we label SVE4 (coral pink). This discrepancy with previous work occurs because the variational states used there (either valley ordered or spin ordered [3]) are too restrictive to find this phase. The spinors that form the ground state in the SVE4 phase are $\cos \frac{\alpha_1}{2} |\hat{e}_x, \uparrow\rangle - \sin \frac{\alpha_1}{2} |-\hat{e}_x, \downarrow\rangle$, $\cos \frac{\alpha_2}{2} |\hat{e}_x, \downarrow\rangle - \sin \frac{\alpha_2}{2} |-\hat{e}_x, \uparrow\rangle$. This phase has nonzero SVEY but vanishing SVEX at $E_v=0$. It may seem that one could rotate the SVEY order parameter to the SVEX order parameter by a combination of a $U(1)_s$ and a $U(1)_v$ rotation. However, recall that we have already used up the $U(1)_s \otimes U(1)_v$ freedom to make the spinors real. The phase SVE4 also manifests nonvanishing CAF and BO order parameters.

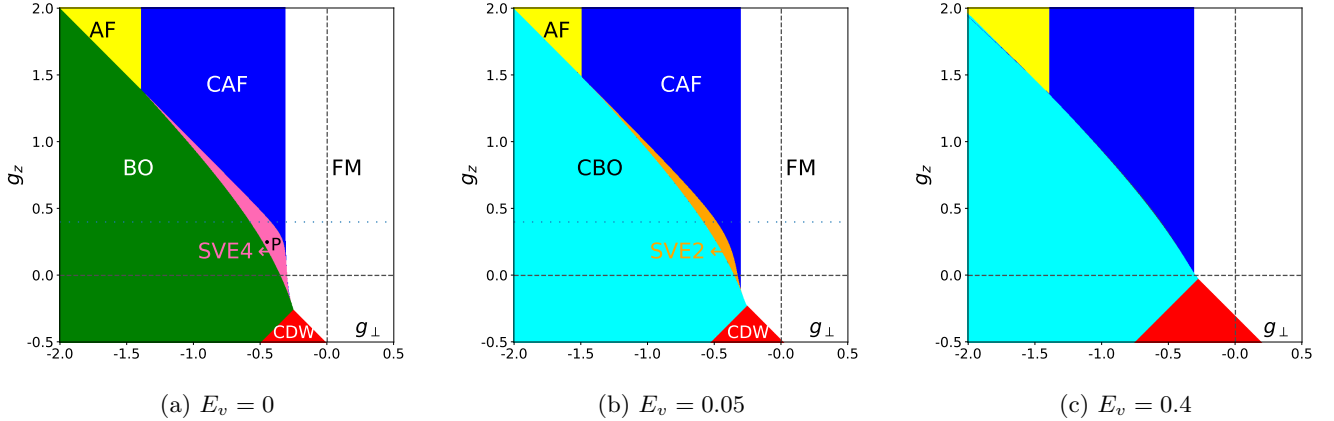


FIG. S2: Phase diagrams for $(1, 2/3, 0, 0)$ and $E_z=1$ in the USR case. (a) For $E_v=0$ we obtain all the previously obtained phases [3], but also a SVE phase (SVE4, coral pink). (b) At small nonzero $E_v=0.05$, the SVE phase changes character to become SVE2. (c) As E_v increases, eventually, the SVE phase disappears.

The states at $E_v=0$ evolve as E_v increases, as seen in Figs. S2a and S2b. The SVE4 phase changes character and becomes the phase we label SVE2 (orange) as soon as $E_v \neq 0$, the difference being that in SVE2 both SVEX and SVEY are nonvanishing. The SVE2 phase shrinks rapidly as E_v increases and vanishes at some critical E_v . Fig. S3 shows three different views of the order parameter evolution. In Fig. S3a we show a section through the $E_v=0$ phase diagram at $g_z=0.4$ as a function of g_\perp . It is clear that the system undergoes a second-order phase transition from the BO phase to the SVE4 phase, and then a first-order transition to the FM phase. Fig. S3b shows

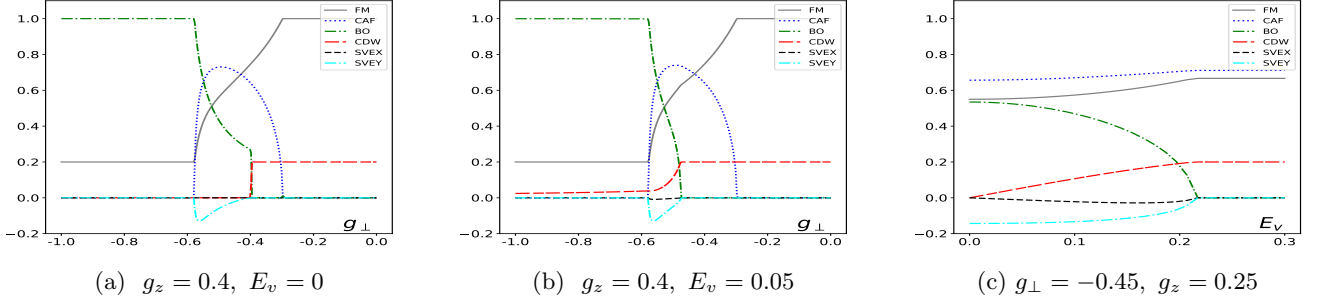


FIG. S3: Different views of order parameter evolution in the USR case for $(1, 2/3, 0, 0)$. (a) A section at $g_z=0.4$ in the phase diagram shown in Fig. S3a. (b) A section at $g_z=0.4$ in the phase diagram shown in Fig. S3b. (c) Order parameters at $g_{\perp} = -0.45, g_z = 0.25$ as functions of E_v . It is seen that the SVE order parameters disappear at $E_v \approx 0.23$.

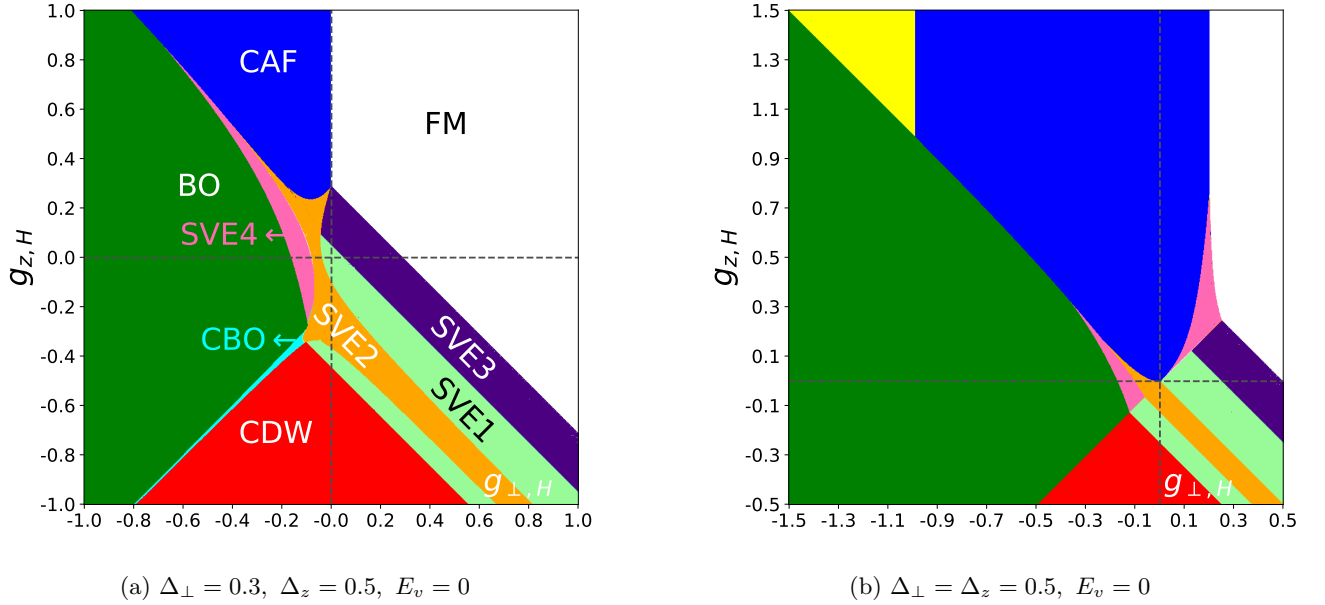


FIG. S4: Phase diagrams with non-USR interactions at $E_z=1, E_v=0$ for $(1, 2/3, 0, 0)$. (a) For Δ_{\perp}, Δ_z tiny CBO appears between the BO and CDW phases. The most striking difference from the USR case is the appearance of four SVE phases. (b) The CBO disappears if we fine-tune to $\Delta_{\perp}=\Delta_z$ but the SVE phases remain.

the same section at $E_v=0.05$. The SVE2 phase has shrunk considerably, and the first-order transition to the FM has become second-order. Fig. S3c shows the evolution of the order parameters with E_v at a specific point in the parameter space $g_{\perp}=-0.45, g_z=0.25$. One sees that as soon as E_v becomes nonzero, the SVEX order parameter also becomes nonzero. At that specific point, the SVE2 phase ceases to be the ground state at around $E_v=0.23$. Now we go beyond USR interactions. When V_1 is turned on, several more phases are found, especially at $E_v=0$ and small E_v . As seen in Fig. S4a, a canted BO (CBO: $|\mathbf{n}_a, \uparrow\rangle, |\mathbf{n}_b, \downarrow\rangle$, in aqua) phase, which is observed at integer fillings only for nonzero E_v , now appears between the BO and CDW phases. The appearance of this phase can be qualitatively understood as the result of the unequal fillings of the two spinors because the charge-ordering fields generated by g_z and the nonzero valley polarization of the two spinors do not cancel. We note that the CBO phase appears only when $\Delta_z \neq \Delta_{\perp}$, as seen from the contrast between Figs. S4b and S4a. In addition, four distinct SVE phases appear in the phase diagram. We have already noted the phases SVE4 and SVE2 in the USR case. The spinors characterizing the new phases are: SVE1: $|K, \uparrow\rangle, \cos(\alpha/2)|K', \uparrow\rangle - \sin(\alpha/2)|K, \downarrow\rangle$ with $\cos \alpha = (2(g_{\perp, H} + g_{z, H} - \Delta_{\perp}) - E_v + E_z)/\Delta_z$ and SVE3: $\cos(\alpha/2)|K, \uparrow\rangle - \sin(\alpha/2)|K', \downarrow\rangle, |K', \uparrow\rangle$ with $\cos \alpha = (4(g_{\perp, H} + g_{z, H} - \Delta_{\perp}) + 3E_v + 3E_z)/6\Delta_z$. The difference between the phases SVE1 and SVE3 is in the

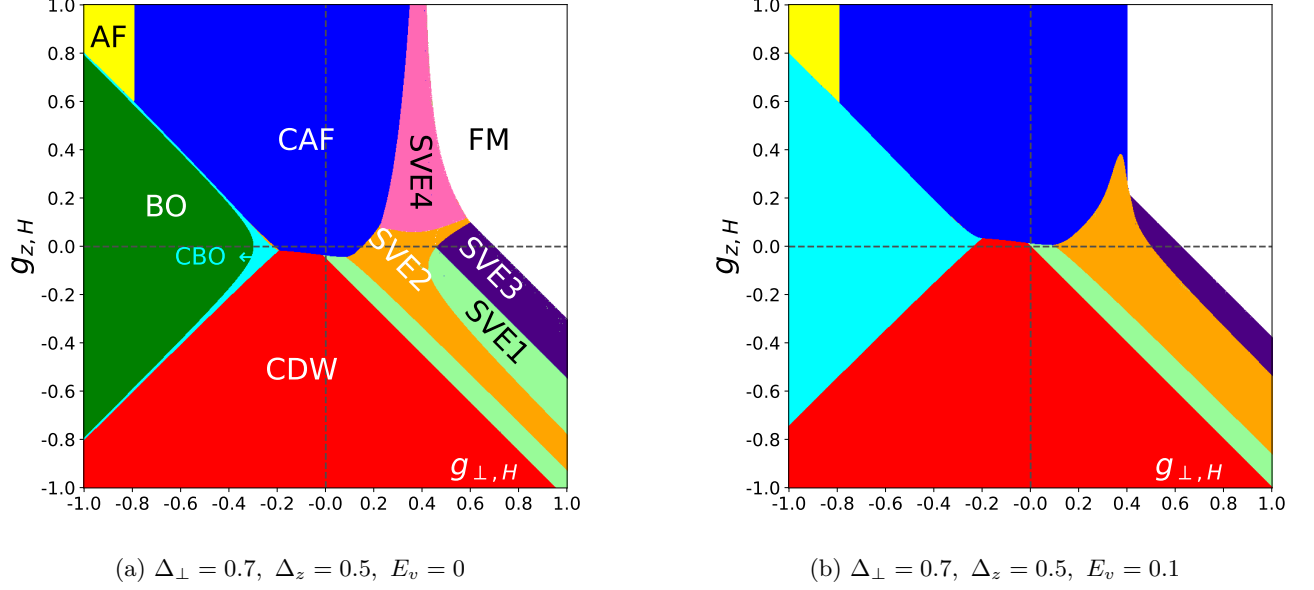


FIG. S5: Phase diagrams at $E_z=1$ for $\Delta_{\perp} > \Delta_z$ for $(1, 2/3, 0, 0)$. (a) A tiny CBO phase appears between the BO and CDW phases at $E_v=0$. This can be understood as a result of the imbalance of the valley ordering energies of the integer and fractional spinors. (b) When a finite E_v is turned on, SVE4 disappears, and the entire BO region becomes CBO, as expected.

relative sign of the order parameters SVEX and SVEY. In phase SVE1, $\langle \tau_x \sigma_x \rangle = \langle \tau_y \sigma_y \rangle$, while in phase SVE3, $\langle \tau_x \sigma_x \rangle = -\langle \tau_y \sigma_y \rangle$.

Fig. S5 shows the evolution of the phase diagram as E_v is turned on. We have already seen in the previous subsection that the phase SVE4 turns into the phase SVE2 upon being subjected to a nonzero E_v . This can also be seen in Figs. S5a and S5b. In fact, SVE2 is seen to take over one region of SVE1 as well. Furthermore, the entire BO phase turns into the CBO phase, which is expected.

SV. PHASE DIAGRAMS FOR $(1, [1, 1]_{-2}, 0) \equiv (1, 1/3, 1/3, 0)$

Let us first recall the USR limit for the filling $(1, 1/3, 1/3, 0)$ shown in Fig. S6a, which was first obtained in Ref. [3]. There are two types of bond-ordered phases, a valley ferromagnet (VFM) state with an $SU(2)$ degeneracy of the valley orientation, a FM phase, a CDW phase, a CAF phase, and an SVE phase, which we label SVE3 (SVE1 & SVE2 have been reported in the main text). Here are the spinors of various phases observed in Fig. S6.

FM: $|K, \uparrow\rangle, |K', \uparrow\rangle, |K', \downarrow\rangle$, AFCDW1: $|K, \uparrow\rangle, |K, \downarrow\rangle, |K', \uparrow\rangle$, BO1: $|-\hat{e}_x, \uparrow\rangle, |\hat{e}_x, \uparrow\rangle, |\hat{e}_x, \downarrow\rangle$, BO2: $|-\hat{e}_x, \uparrow\rangle, |\hat{e}_x, \uparrow\rangle, |-\hat{e}_x, \downarrow\rangle$, CBO: $|-\mathbf{n}_a, \uparrow\rangle, |\mathbf{n}_a, \uparrow\rangle, |\mathbf{n}_b, \downarrow\rangle$, VFM: $|\mathbf{n} = \hat{e}_x, \uparrow\rangle, |K, \downarrow\rangle, |K', \downarrow\rangle$, CAF: $|K, \mathbf{s}_a\rangle, |K, -\mathbf{s}_a\rangle, |K', \mathbf{s}_b\rangle$, and SVE3: $|\hat{e}_x, \mathbf{s}_a\rangle, |\hat{e}_x, -\mathbf{s}_a\rangle, |-\hat{e}_x, \mathbf{s}_b\rangle$. Here $\mathbf{n}_a, \mathbf{n}_b, \mathbf{s}_a, \mathbf{s}_b$ in each phase are determined by minimization.

Going beyond USR interactions, interestingly, when $\Delta_z = \Delta_{\perp}$, the observed phases are the same as those in the USR case, with slightly different domains. This indicates that there is perhaps some hidden symmetry in the model for $\Delta_z = \Delta_{\perp}$, which we intend to explore in the near future [9]. However, when $\Delta_z \neq \Delta_{\perp}$, two new phases appear, a canted bond-ordered phase (CBO, in aqua) and a second SVE phase (SVE2, in light blue). Furthermore, the nature of some of the phases depends on which Δ is larger. In Fig. S6c, we present the case $\Delta_{\perp} < \Delta_z$. The valley direction of the VFM is now pinned to be equatorial, making it the BO3 phase. For $\Delta_{\perp} > \Delta_z$, as seen in Fig. S7a, the valley direction gets pinned to be polar leading to the AFCDW2 phase: $|K, \uparrow\rangle, |K, \downarrow\rangle, |K', \downarrow\rangle$. Fig. S7b shows how the phase diagram of Fig. S7a evolves at nonzero E_v . The CBO and SVE2 phases disappear.

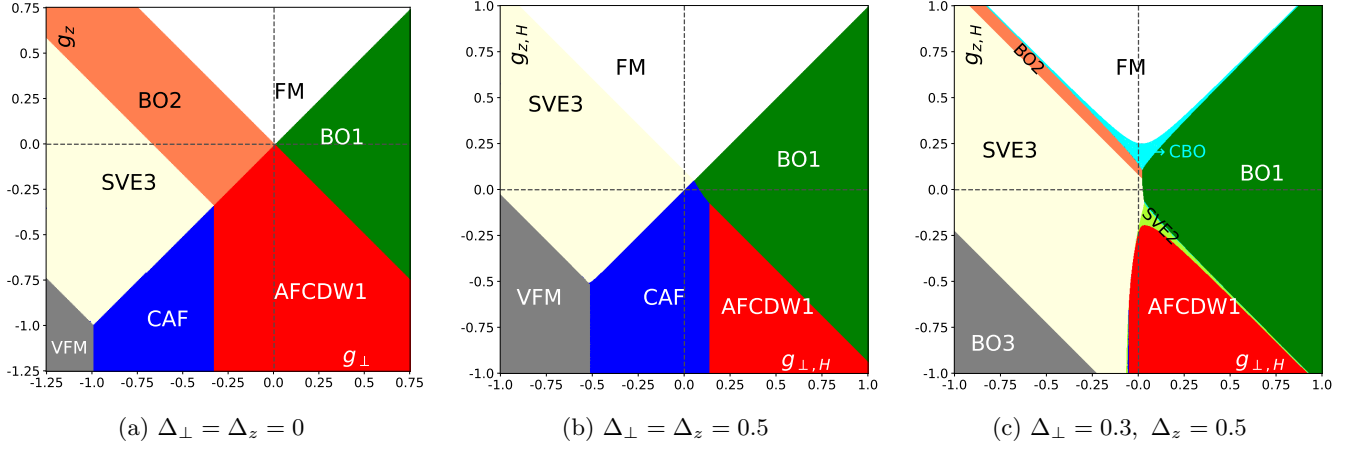


FIG. S6: Phase diagrams for the state $(1, \frac{1}{3}, \frac{1}{3}, 0)$ at $E_z=1$, $E_v=0$. (a) In the USR limit, as described in Ref. [3]. (b) Phase diagram for fine-tuned $\Delta_{\perp} = \Delta_z$. The nature and overall topology remain the same. The phase BO2 has shrunk to zero. (c) Phase diagram for $\Delta_{\perp} < \Delta_z$. The VFM changes character to become bond-ordered (BO3), with the \mathbf{n} vector of the VFM state becoming equatorial. Also, a CBO phase and a SVE phase appear at the boundaries of the old phases.

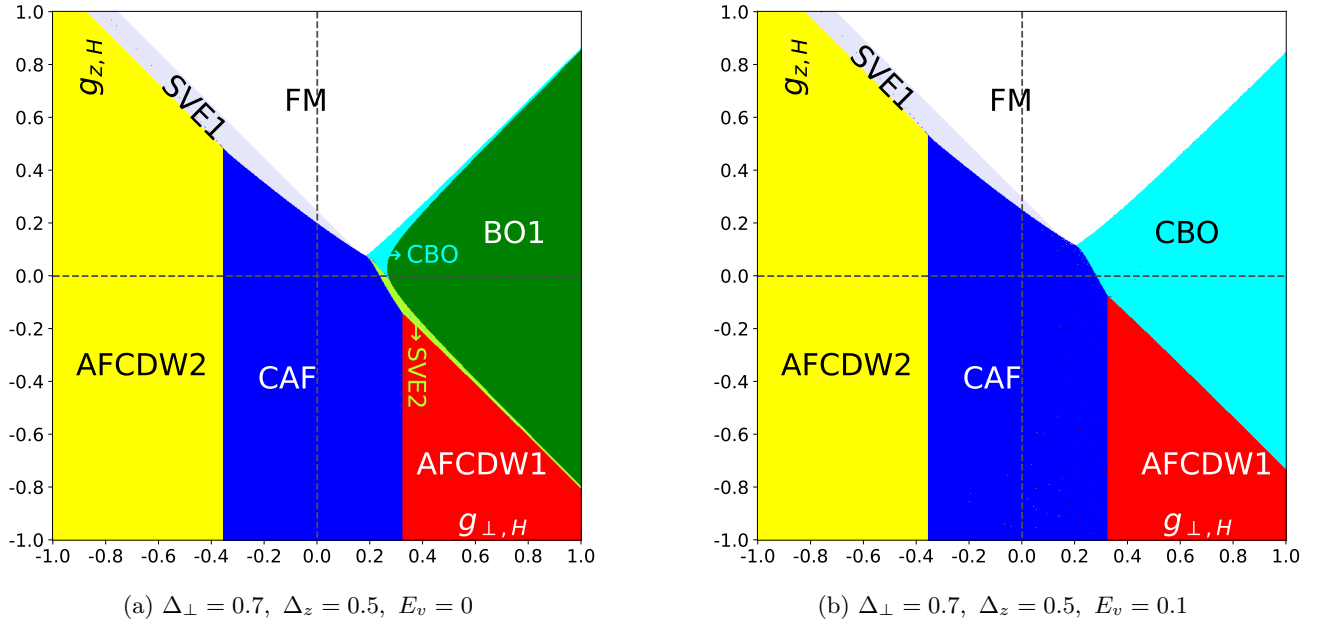


FIG. S7: Phase diagrams of $(1, 1/3, 1/3, 0)$ at $E_z=1$ for $\Delta_{\perp} > \Delta_z$. (a) At $E_v=0$ the valley ordering vector of the VFM phase in the USR case gets pinned to the polar direction, making this phase the AFCDW2 phase. Further, three new phases that did not occur for the USR case appear: SVE1, SVE2, and CBO. (b) When E_v is turned on, the CBO and SVE2 phases disappear.

SVI. COULOMB PHASE DIAGRAM OF TWO- AND THREE-COMPONENT STATES

As mentioned in the main text, once one considers the Coulomb interaction, there can be transitions between 2CS and 3CS states driven by the different scaling of the Coulomb and short-range interaction strengths with B_{\perp} , or the dielectric screening κ . We will carry out this exercise for the states $(1, 2/3, 0, 0)$ and $(1, 1/3, 1/3, 0)$. The Coulomb energy difference between these two states is determined solely by their fractional parts [3], i.e.

$$\delta E^C = E_{(1, \frac{2}{3}, 0, 0)}^C - E_{(1, \frac{1}{3}, \frac{1}{3}, 0)}^C = E_{\frac{2}{3}}^C - E_{(\frac{1}{3}, \frac{1}{3})}^C, \quad (\text{S15})$$

where $E_{\frac{2}{3}}^C$ and $E_{(\frac{1}{3}, \frac{1}{3})}^C$ are obtained via exact diagonalization[10].

$$E_{\frac{2}{3}}^C = \frac{2}{3} \times (-0.51829) \frac{e^2}{\kappa \ell_B}, \quad E_{(\frac{1}{3}, \frac{1}{3})}^C = \frac{2}{3} \times (-0.52704) \frac{e^2}{\kappa \ell_B}, \quad (\text{S16})$$

where $\ell_B = \sqrt{\hbar c / e B_{\perp}}$ is the magnetic length. The relative dielectric constant of graphene depends on the encapsulating conditions and is typically in the range $4 < \kappa < 8$. We choose to illustrate the competition between the 2CS and 3CS states at $B=10$ Tesla. At this field, the Zeeman energy is $E_z = (1/2)g\mu_B B = 0.58$ meV [$g=2$ for graphene], and the bare Coulomb energy (sans the dielectric constant) is $e^2/\ell_B = 182$ meV. We then express all energies in units of E_z , i.e., we set $E_z=1$. Therefore, $\delta E^C = E_{\frac{2}{3}}^C - E_{(\frac{1}{3}, \frac{1}{3})}^C = 1.84/\kappa$. To decide which state prevails, we compute the total energy difference

$$\Delta E = E_{(1, \frac{2}{3})}^{\text{an}} - E_{(1, \frac{1}{3}, \frac{1}{3})}^{\text{an}} + \delta E^C. \quad (\text{S17})$$

In Fig. S8 we show the results for $\kappa=4, 6, 8$ for the non-USR interactions characterized by $\Delta_{\perp}=0.7$, $\Delta_z=0.5$. The leftmost column of the two panels shows the phase diagrams of the 2CS and 3CS. In each column of panels, if the energy of the 2CS/3CS state is lower than its competitor in a particular region of the parameter space, it is shown in color, whereas if its energy is higher than its competitor, the region is colored black. As expected, it is seen that for large anisotropic couplings, the anisotropy energy of the 2CS can overwhelm the Coulomb energy advantage of the 3CS. As the screening increases, the Coulomb energy advantage of the 3CS shrinks, and its region of appearance in the phase diagram also shrinks.

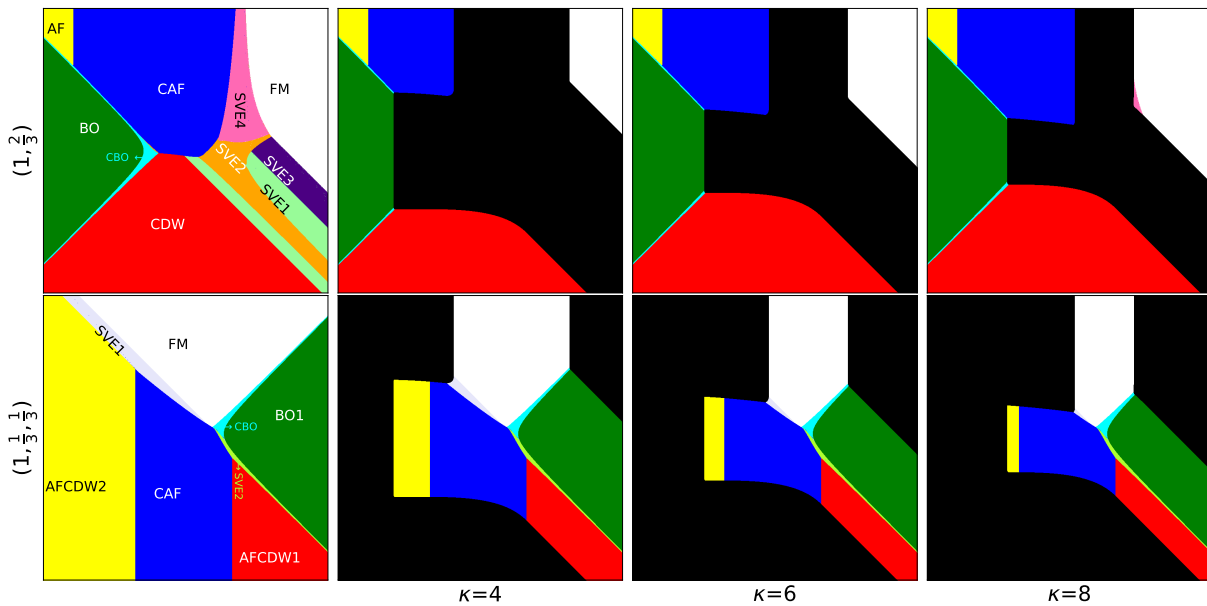


FIG. S8: The competition between the two- and three-component states at $\nu=-2+5/3$, including the Coulomb and residual anisotropy energies for $\Delta_{\perp}=0.7$, $\Delta_z=0.5$. The leftmost vertical panels are the phase diagrams of the 2CS (top) and 3CS (bottom) states. Each successive set of two vertically aligned panels shows the regions where each type of state has lower energy (in color in the corresponding phase diagram) or higher energy (in black). The three sets of panels are for $\kappa=4, 6, 8$ respectively.

-
- [1] F. D. M. Haldane, Fractional quantization of the Hall effect: A hierarchy of incompressible quantum fluid states, *Phys. Rev. Lett.* **51**, 605 (1983).
 - [2] B. Douçot, M. O. Goerbig, P. Lederer, and R. Moessner, Entanglement skyrmions in multicomponent quantum Hall systems, *Phys. Rev. B* **78**, 195327 (2008).
 - [3] I. Sodemann and A. H. MacDonald, Broken SU(4) symmetry and the fractional quantum Hall effect in graphene, *Phys. Rev. Lett.* **112**, 126804 (2014).

- [4] Y. Lian, A. Rosch, and M. O. Goerbig, SU(4) skyrmions in the $\nu = \pm 1$ quantum Hall state of graphene, [Phys. Rev. Lett. **117**, 056806 \(2016\)](#).
- [5] Y. Lian and M. O. Goerbig, Spin-valley skyrmions in graphene at filling factor $\nu = -1$, [Phys. Rev. B **95**, 245428 \(2017\)](#).
- [6] J. Atteia, Y. Lian, and M. O. Goerbig, Skyrmion zoo in graphene at charge neutrality in a strong magnetic field, [Phys. Rev. B **103**, 035403 \(2021\)](#).
- [7] J. Atteia and M. O. Goerbig, SU(4) spin waves in the $\nu = \pm 1$ quantum Hall ferromagnet in graphene, [Phys. Rev. B **103**, 195413 \(2021\)](#).
- [8] S. J. De, A. Das, S. Rao, R. K. Kaul, and G. Murthy, Global phase diagram of charge-neutral graphene in the quantum Hall regime for generic interactions, [Phys. Rev. B **107**, 125422 \(2023\)](#).
- [9] Work in progress.
- [10] A. C. Balram, C. Töke, A. Wójs, and J. K. Jain, Fractional quantum Hall effect in graphene: Quantitative comparison between theory and experiment, [Phys. Rev. B **92**, 075410 \(2015\)](#).